Journal of Materials Chemistry A

PAPER

View Article Online
View Journal | View Issue

Cite this: J. Mater. Chem. A, 2016, 4, 17381

A nitrogen–sulfur co-doped porous graphene matrix as a sulfur immobilizer for high performance lithium–sulfur batteries†

Jing Xu,‡[a] Dawei Su,‡[a] Wenxue Zhang,[ab] Weizhai Bao[a] and Guoxiu Wang*[ac]

Received 13th July 2016
Accepted 4th October 2016

DOI: 10.1039/c6ta05878g

www.rsc.org/MaterialsA

Owing to their overwhelming advantage of theoretical energy density, lithium–sulfur (Li–S) batteries are considered as one of the most promising candidates for next-generation electrochemical energy storage systems. The primary challenges in the development of Li–S batteries include the suppression of the polysulfide shuttle effect and maintenance of high sulfur loading. Herein, we report a strategy of strong chemisorption for polysulfides utilizing a chemically activated graphene matrix co-doped with nitrogen and sulfur. The dopant N and S atoms act as electron attracting atoms, leading to the nearby C atoms and causing oxygen functional groups to be polarized and more active for anchoring sulfur and polysulfides. Meanwhile, highly developed defects and edges, as well as the porous structure derived from graphene chemical activation, not only achieve a high sulfur loading in a well dispersed amorphous state, but also serve as polysulfide reservoirs to alleviate the shuttle effect. When applied as cathode hosts for lithium–sulfur batteries, the nitrogen–sulfur co-doped porous graphene architecture exhibited a high specific capacity of 1178 mA h g^{-1} at 0.2C, 1103 mA h g^{-1} at 0.5C, and 984 mA h g^{-1} at 1C rate, and excellent cycling stability for 600 cycles with a retained capacity of 780 mA h g^{-1} (0.2C).

Introduction

The rapid depletion of fossil fuels and increasing environmental pollution issues are the major stimulating forces for the development of clean energy technologies. Renewable energy sources, such as solar, wind, and tide, are attractive in this regard. However, efficient utilization of these intermittent resources requires efficient and economical energy storage (EES) systems. Advanced rechargeable batteries are the most suitable option for EES. However, confined by their limited theoretical energy density, as well as high cost, state-of-the-art lithium-ion batteries (LIBs) are not capable of fulfilling the specific energy requirements for future electric vehicles (EVs) and large-scale smart grid applications. Therefore, it is of great importance to develop advanced rechargeable batteries to satisfy future needs. Invented in the 1960s, rechargeable lithium–sulfur batteries have now attracted extensive interest, mainly due to their high theoretical energy density ($\approx$2567 W h kg^{-1}), which is estimated to be 5 times higher than that of state-of-the-art lithium-ion batteries. Due to the natural abundance, low cost and environmental friendliness, Li–S batteries are one of the most promising rechargeable battery technologies for a wide range of applications.[1–5]

Despite considerable advantages of lithium–sulfur batteries, their commercialization still suffers from some tough obstacles, such as the insulating nature of sulfur, large volume expansion/contraction (~80%) during cycling, dissolution of polysulfides (Li_2S_x, $4 \leq x \leq 8$) in organic electrolytes, and the shuttle effect of polysulfides, which inevitably result in the low electrochemical utilization of sulfur and rapid capacity degradation.[2,6–10] Many approaches have been devoted to addressing these issues. These include: (1) encapsulating sulfur particles into various carbon matrix materials and/or conducting polymers, such as mesoporous carbon, carbon nanofiber interlayers, and reduced graphene oxide, polyaniline (PAni), polypyrrole (PPy), and their derivatives.[3,4,8,11,12] (2) Strengthening sulfur's chemical bonds *via* chemical interactions or surface-mediated redox reactions with metal oxides (*e.g.* SiO_2, TiO_2, metal–organic frameworks) and metal carbides (MXene phases).[13,16,18] (3) Adding novel electrolyte additives such as P_2S_5 or Cs^+ to suppress the polysulfide shuttle.[17,19] (4) Modifying the surface chemistry of the hosts to prevent the shuttle effect of the soluble polysulfides between the cathode and the anode, enabling better cycling performance.[20,22] The chemical properties of sp^2 carbon materials can be further modified by introducing heteroatom doping, such as phosphorus, sulfur, boron and nitrogen, which demonstrated significant potential for lithium polysulfide confinement.[9] Song *et al.*

[a]Centre for Clean Energy Technology, School of Mathematical and Physical Sciences, Faculty of Science, University of Technology Sydney, NSW 2007, Australia. E-mail: Guoxiu.Wang@uts.edu.au

[b]School of Materials Science and Engineering, Chang'an University, Xi'an 710064, China

[c]College of Materials Science and Technology, Nanjing University of Aeronautics and Astronautics, Nanjing, Jiangsu 210016, China

† Electronic supplementary information (ESI) available. See DOI: 10.1039/c6ta05878g

‡ Jing Xu and Dawei Su contributed equally to this work.

reported that nitrogen doping in mesoporous carbon effectively promoted the chemical adsorption of sulfur atoms on oxygen-containing functional groups because surface modification with nitrogen atoms greatly enhances the electrochemical reactivity and electronic conductivity of carbon matrices.[14,51] Additionally, sulfur-doped porous carbon also attracted wide attention for battery applications due to the fact that sulfur-doping can change the charge state of the neighbouring carbon atoms. Therefore, sulfur-doped carbon materials exhibit enhanced adsorption ability. Most importantly, when sulfur and nitrogen are simultaneously doped into the carbon matrix, synergistic effects can occur due to the highly active multiple doping elements.[15,21,24,26] The co-doping not only strengthens the chemical bonding between the carbon host and sulfur chains in the heat treatment during the sulfur loading process, ensuring the uniform distribution of sulfur, but also generates more active sites and increases their activity, which greatly improve the adsorption of soluble lithium polysulfide intermediates, thus increasing the cycle ability and coulombic efficiency.[29] Therefore, the co-doping strategy can achieve superior electrochemical activity beyond that of mono-element doping.

Graphene, a free-standing atom-thick layer of sp^2 carbon atoms, has emerged as the most significant carbon material in the last decade due to its unique physical and chemical properties.[23,25,41,42,53–55] Nitrogen–sulfur co-doped graphene is a promising nanoscale immobilizer as a cathode host material for lithium–sulfur batteries. However, graphene nanosheets tend to form agglomerates or even restack through van der Waals interactions during the preparation processes and subsequent electrode fabrication,[27] resulting in the loss of specific surface area. This effect will also lead to lower polysulfide adsorption due to the decrease of the accessible active sites on the graphene surface. Therefore, it is very important to prevent graphene aggregation by creating a porous structure of nitrogen–sulfur co-doped graphene nanosheets.

Herein, we have developed a highly crumpled nitrogen–sulfur co-doped 3D graphene nanosheet matrix as a sulfur immobilizer for lithium–sulfur batteries. These highly porous nitrogen–sulfur co-doped graphene nanosheets were synthesized through a facile synthesis approach, in which polypyrrole (PPy) serves as a nitrogen source and ammonium persulfate (APS) as a sulfur source. Highly developed defects and edges, as well as hierarchical pore structures derived from graphene chemical activation endow nitrogen–sulfur co-doped graphene nanosheets with large surface area (1012 $m^2\ g^{-1}$) and a wide pore size distribution of 2 nm and 25–40 nm. The as-prepared materials have strong chemisorption capabilities for polysulfides and high sulfur loading. When applied as cathode materials in lithium–sulfur batteries, the cathodes exhibit a high initial capacity of 1178 mA h g^{-1} at 0.2C and excellent long life cycling performance with a retained capacity of 780 mA h g^{-1} after 600 cycles.

Experimental

Synthesis of NSG

Graphene oxide (GO) was synthesized using natural graphite flakes by a modified Hummers' method. 50 mg of the as-made graphene oxide was well suspended in 50 mL DI water after ultrasonically stirring for 2 h, then 0.73 g cetyltrimethylammonium bromide (CTAB) and 1.37 g ammonium persulfate (APS) were dissolved into the prepared graphene solution magnetic stirring for 1 h. After that, 0.83 mL of 99% pyrrole monomer was added and the mixture was stirred in an ice water bath for about 24 h. When the reaction finished, the resultant products were washed with DI water and dried in a vacuum at 80 °C for 24 h to remove any residual solvents, this final product is denoted as NSG.

Synthesis of A-NSG

Typically, 400 mg NSG powder was dispersed in 20 mL 3 M K_2CO_3 solution and stirred for 24 hours. The extra K_2CO_3 solution was removed by briefly filtering the mixture through a polycarbonate membrane (Whatman, 0.2 μm); then the mixture was dried in the lab environment at 70 °C for 24 hours. The NSG/K_2CO_3 mixture was put in a tube furnace under flowing nitrogen at 800 °C for 2 h (heating rate 5 °C min^{-1}). Subsequently, the final product (denoted as A-NSG) was thoroughly washed with 0.1 M HCl and DI water until the pH value reached 7 and finally dried in a vacuum at 80 °C for 20 h.

Synthesis of A-NSG@S

A-NSG was homogeneously dispersed in DI water by ultrasonication, then transferred to an appropriate amount of elemental sulfur/CS_2/ethanol solution with a mass ratio of $m_{\text{A-NSG}} : m_S = 1 : 3$, the mixed solution was magnetically stirred for 24 h over an ice water bath. During this time period, the CS_2 and ethanol were allowed to completely evaporate while stirring, then the A-NSG@S composite was filtered and dried at 50 °C in a vacuum oven for 12 h. Finally, the as-synthesized A-NSG@S was heated to 155 °C at a heating rate of 2 °C min^{-1} in a tube furnace under flowing argon at 100 sccm before reheating at 230 °C for another 2 h under the same conditions.

Characterization of materials

The morphology of the obtained materials was characterized by field emission scanning electron microscopy (FESEM, Zeiss Supra 55VP) and transmission electron microscopy (TEM, Model JEM-2011, JEOL). The crystallographic information for the samples was collected on a Siemens D5000 diffractometer using Cu-K radiation with a scanning step of 0.02° per second. Raman spectra were measured by a Renishaw in Via Raman spectrometer system (Gloucestershire, UK) equipped with a Leica DMLB microscope (Wetzlar, Germany) and a 17 mW 633 nm Renishaw helium neon laser at 50% power. XPS analysis was performed on an ESCALAB MK II X-ray photoelectron spectrometer. FTIR spectra were recorded on a NEXUS 670FTIR spectrometer using KBr disks. Thermogravimetric analysis (TGA) was used for the analysis of weight loss from the precursor to the final product. Nitrogen adsorption–desorption measurements were conducted on a 3 Flex surface characterization analyzer to determine the Brunauer–Emmett–Teller (BET) specific surface area using a Quadrasorb SI analyzer at 77 K. The BET surface area was calculated using experimental

points at a relative pressure of P/P_0 = 0.05–0.25. The UV-vis spectra were measured in the spectral range of 300–1000 nm using a Cary 60 UV-vis variable wavelength spectrophotometer. All the samples for UV-vis measurement were prepared and sealed in an argon-filled glove box.

Electrochemical characterization

Working electrodes were made from 90 wt% of active materials, 2 wt% of conductive agent (carbon black) and 8 wt% of binder (polyvinylidene difluoride). The mass loading of sulfur on the electrode is around 1.5 mg cm^{-2}. CR2032 coin cells were assembled in an argon-filled glove box (Mbraun, Unilab, Germany), in which both the moisture and oxygen contents were controlled to be less than 0.1 ppm. Lithium foil was used as a counter electrode. The electrolyte was 1 M lithium bis(trifluoromethanesulfonyl) imide (LiTFSI) and 1 wt% lithium nitrate ($LiNO_3$) in 1,3-dioxolane and 1,2-dimethoxy-ethane (volume ratio 1 : 1), for each electrode, around 30 μL electrolyte was added into the coin cell. The electrodes were dried at 60 °C under vacuum for 12 h. Electrochemical measurements were conducted using a LAND-CT2001C battery test system. The cells were discharged and charged galvanostatically in the fixed voltage range of 1.7–2.7 V with a current rate of 0.1C, 0.5C, 1C, 2C, and 5C. Cyclic voltammetry (CV) and electrochemical impedance spectroscopy (EIS) were conducted with a CHI660C electrochemistry workstation in the voltage range of 1.7 to 2.7 V (*vs.* Li^+/Li).

Computational methods

The simulations are based on density functional theory (DFT), which is provided by DMOL3. The generalized gradient approximation (GGA) with the Perdew–Burke–Ernzerhof scheme (PBE) is adopted for the exchange–correlation potential to optimize geometrical structures and calculate properties. The All-Electron Relativistic Kohn–Sham wave functions (AER) and double numeric plus polarization (DNP) basis set are adopted in the local atomic orbital basis set with the global orbital cutoff set to 4.4 Å. A single-layer of graphene was modelled using a hexagonal 4 × 4 supercell. The nearest distance between nanosheets in neighboring cells is greater than 15 Å to ensure no interactions between different layers. For geometric optimization, both the cell and the atomic positions are allowed to fully relax. The Brillouin zone is sampled at 6 × 6 × 1 *k*-points for all structures in the geometric optimization calculations, which brings out the convergence tolerance of energy of 1.0×10^{-5} Ha (1 Ha = 27.2114 eV), maximum force of 0.002 Ha per Å, and maximum displacement of 0.005 Å. The adsorption energy (E_a) is defined as:

$$E_a = E_{total} - E_{ads} - E_{substrate}$$

where E_{total} is the total energy of the adsorbed system, E_{ads} is the energy of the adsorbate in vacuum and $E_{substrate}$ is the energy of the doped and undoped graphene substrate. According to this definition, a more negative value indicates a more energetically favorable (exothermic) reaction between polysulfides and the graphene surface.

Results and discussion

The 3D nitrogen–sulfur co-doped porous graphene matrix was synthesized *via* chemical activation of polypyrrole (PPy) functionalized graphene sheets using K_2CO_3 as shown in Scheme 1. PPy was chosen as the nitrogen source due to its high nitrogen content. More importantly, because of the π–π interaction between PPy and graphene oxide (GO), the PPy monomers will polymerize on the surfaces of graphene oxide (GO) during the polymerization process. The doping of sulfur was achieved by ammonium persulfate (APS). After carbonization, nitrogen and sulfur atoms are expected to dope in the graphene nanosheets. Scanning electron microscopy (SEM) images of nitrogen and sulfur co-doped graphene (denoted as NSG) composites are shown in Fig. S1 (ESI†), it is clear that the NSG composites show quite similar morphologies to the rGO, displaying a thin smooth surface. The as-prepared NSG was chemically activated by K_2CO_3 to obtain final porous nitrogen–sulfur co-doped graphene (denoted as A-NSG). Fig. 1a, 2a and S2 (ESI†) show the scanning electron microscopy (SEM) images and transmission electron microscopy (TEM) images of A-NSG. The corrugated morphology with wrinkles and folded regions is clearly visible, which is markedly different from rGO and NSG. Meanwhile, most of the A-NSG layers are discontinuous, giving rise to a large number of defects such as edges and pores. Fig. 1d shows the typical AFM image of the A-NSG, which further reveals that the thin wall typically consists of only a few graphene layers as the A-NSG nanosheets with an average thickness of about 0.396 nm. The crumpling of the A-NSG can effectively prevent them from agglomerating and restacking, thus increasing the electrolyte accessible surface area. The corresponding energy-dispersive X-ray spectroscopy (EDX) illustrates uniform distribution of carbon, nitrogen and sulfur in A-NSG (Fig. 1b).

Applying the 3D A-NSG hierarchical network structure as the sulfur host, we loaded sulfur into the A-NSG matrix by liquid-phase infiltration and melt vulcanization processes. The initial liquid phase infiltration process ensures the uniform distribution of sulfur in the A-NSG. The melt vulcanization processes include two major steps: (i) a typical step at 155 °C for 10 hours, aiming to encapsulate sulfur into the porous graphene 3D frameworks (denoted as A-NSG@S-155), and (ii) heating at 230 °C, to trigger the ring-opening polymerization of elemental sulfur (S_8) into linear polysulfides along porous graphene (denoted as A-NSG@S-230). In the A-NSG@S composites, a uniform layer of sulfur is homogeneously anchored on the surface of A-NSG without any obviously aggregated sulfur particles being observed in the TEM image (Fig. 2c) or FSEM image (Fig. 1c). The sulfur content in the A-NSG@S nanocomposites was determined by thermogravimetric analysis (TGA) under a nitrogen atmosphere with a heating rate of 10 °C min^{-1}, as shown in Fig. S3 (ESI†). The TGA analyses reveal that the sulfur loading in A-NSG@S was 72.4 wt%, thus the mass loading of sulfur in each electrode is around 65%. To verify the structural characteristics of A-NSG@S, X-ray diffraction (XRD) was conducted on pure sulfur, A-NSG@S-155, and A-NSG@S-230 (Fig. 3a). It should be noted that the overlapped broad peak

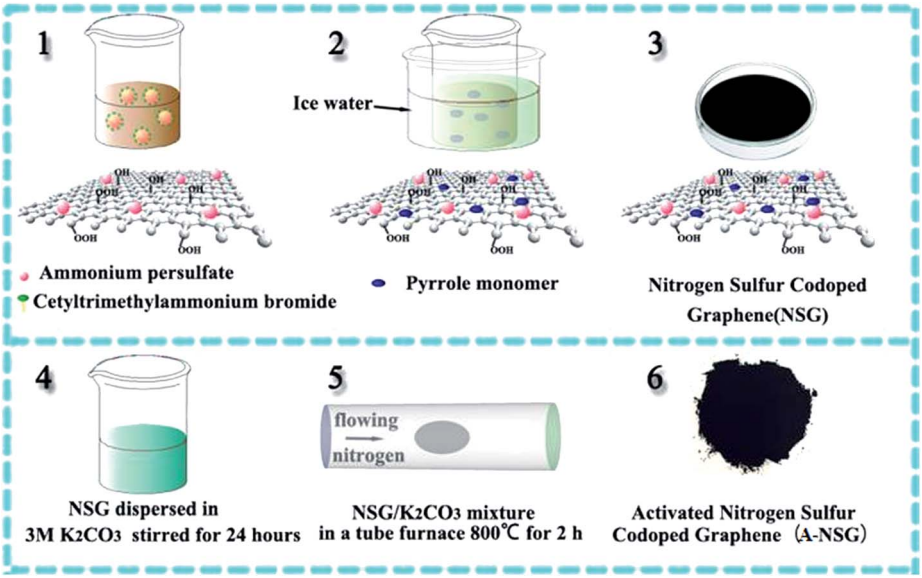

Scheme 1 Schematic illustration of the formation of A-NSG.

at about 26° appear in both A-NSG@S-155 and A-NSG@S-230, which can be ascribed to the A-NSG from thermal restoration of sp^2 carbon.[21] Compared with the intact crystalline peaks of pure sulfur and A-NSG@S-155, the absence of sulfur crystal peaks for A-NSG@S-230 is noteworthy (Fig. 3a). This indicated that sulfur now exists in a highly dispersed amorphous state. Meanwhile, as shown in the Raman spectra (Fig. 3b), the pure sulfur powder exhibits characteristic peaks in the range of 100–500 cm^{-1}, associated with the vibration of the S–S bond in S_8 species while both the A-NSG@S-155 and A-NSG@S-230 did not show noticeable characteristic sulfur peaks, which is also consistent with the conclusion from XRD patterns.[28] Additionally, the SAED pattern (Fig. S4, ESI†) of A-NSG@S reveals a typical sixfold symmetry expected for graphene without any sign of crystallized sulfur, confirming its amorphous state. This implies that S_8 molecules were loaded into the A-NSG matrix without long-range ordering, similar to small sulfur molecule dispersion. Other groups have reported that the amorphous state of sulfur

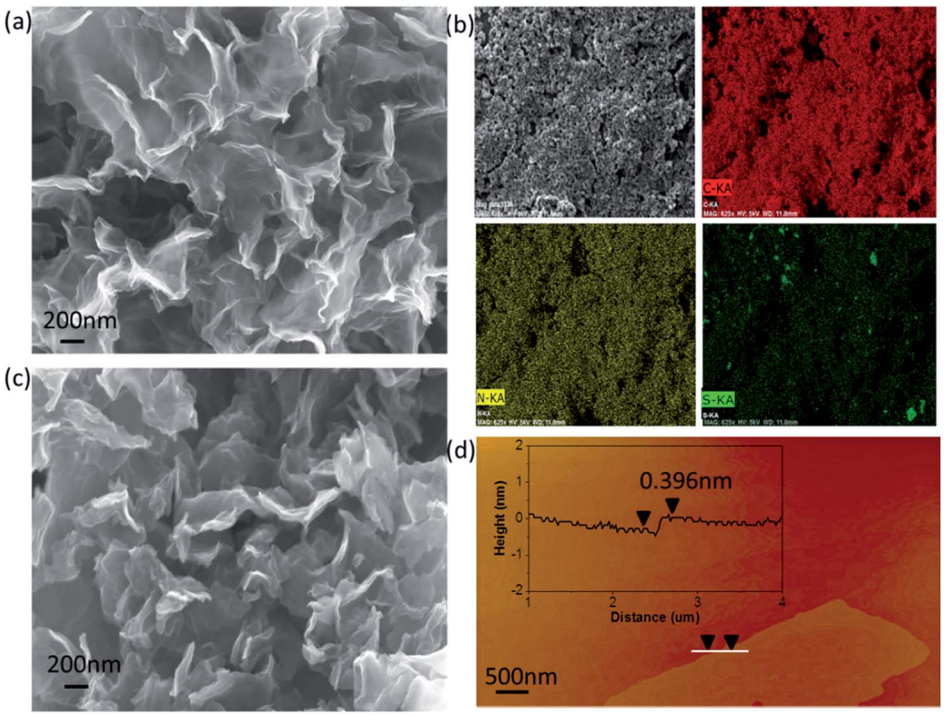

Fig. 1 (a) SEM image of A-NSG. (b) EDX elemental mapping for A-NSG. (c) SEM image of the A-NSG@S. (d) AFM image of A-NSG.

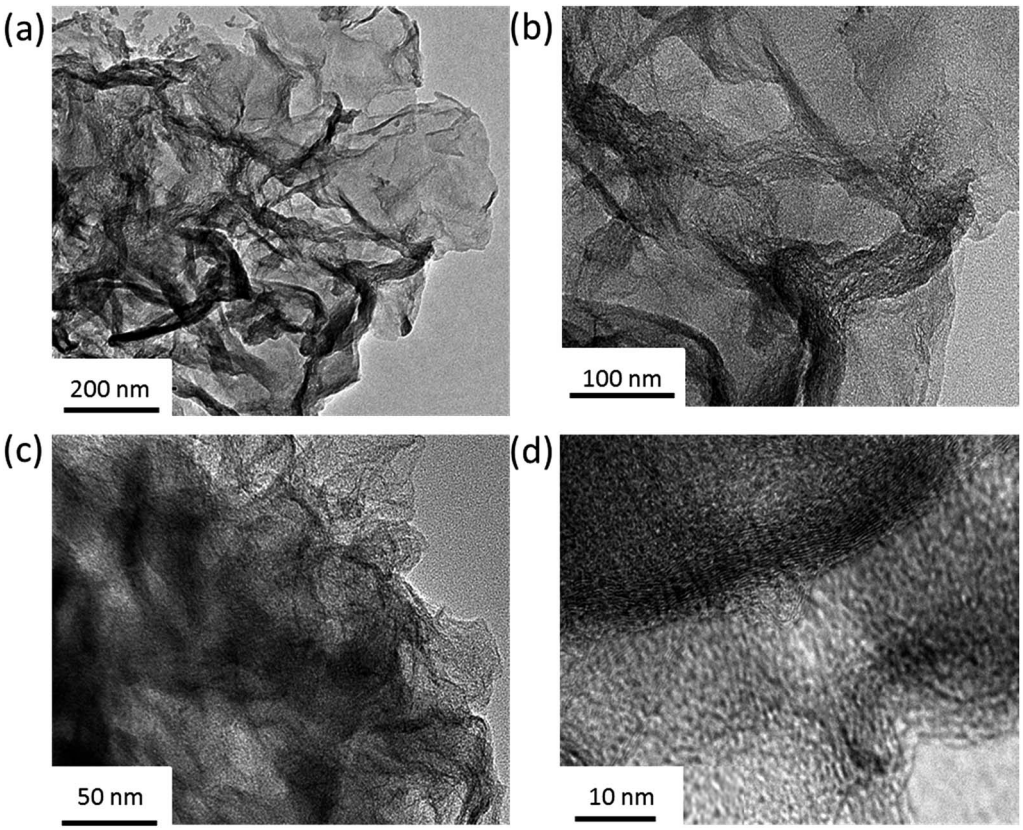

Fig. 2 (a and b) TEM images of A-NSG. (c and d) High-magnification TEM images of the A-NSG@S.

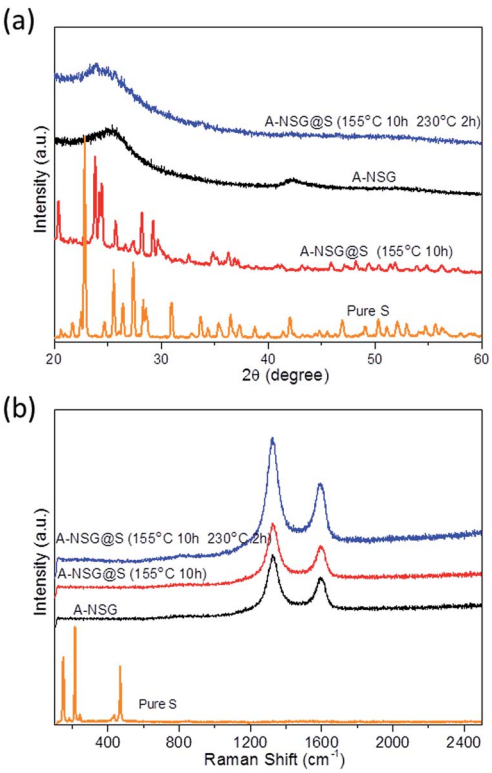

Fig. 3 XRD patterns and Raman spectra of the pure sulfur powder, A-NSG, A-NSG@S-155, and A-NSG@S-230.

could result in the high utilization of sulfur in electrochemical lithiations.[23]

To investigate the elemental composition and functional groups in the A-NSG, X-ray photoelectron spectroscopy (XPS) measurements were performed. As shown in Fig. 4a, the XPS survey spectrum of A-NSG exhibits four characteristic peaks located at *ca.* 164, 400.23, 285.07 and 532.25 eV, corresponding to S 2p, N 1s, C 1s, and O 1s. The elemental content of S and N in A-NSG is 0.85 at% and 4.18 at%, respectively. This suggests the effective doping of N and S into the graphene sheets. In the N 1s spectrum of A-NSG (Fig. 4b), three components including pyridinic N (21.68 wt%), pyrrolic N (50.16 wt%), and graphitic N (28.16 wt%), can be identified at 398.4, 400.2 and 402.1 eV, respectively.[22,30] It is also reported that the dominant pyridinic and pyrrolic N had been proven to contribute to the improvement of the affinity and binding energy of non-polar carbon atoms with polar and rate capability of Li–S batteries.[7,22] We also displayed the molecular geometries and the adsorption energies of Li_2S and Li_2S_4 on pyridinic and pyrrolic N sites in Fig. S5a–d (ESI†). In the most stable configuration, terminal Li atoms in Li_2S and Li_2S_4 tended to directly bind to the pyridinic N atom. There was distinctive electron concentration between N and Li atoms, suggesting a strong Li–N electrostatic interaction. The electron migration can be well explained by the Lewis acid–base theory.[43,44] The pyridinic N with an extra pair of electrons was considered as an electron-rich donor that naturally acted as a Lewis-base site to interact with the strong Lewis acid of

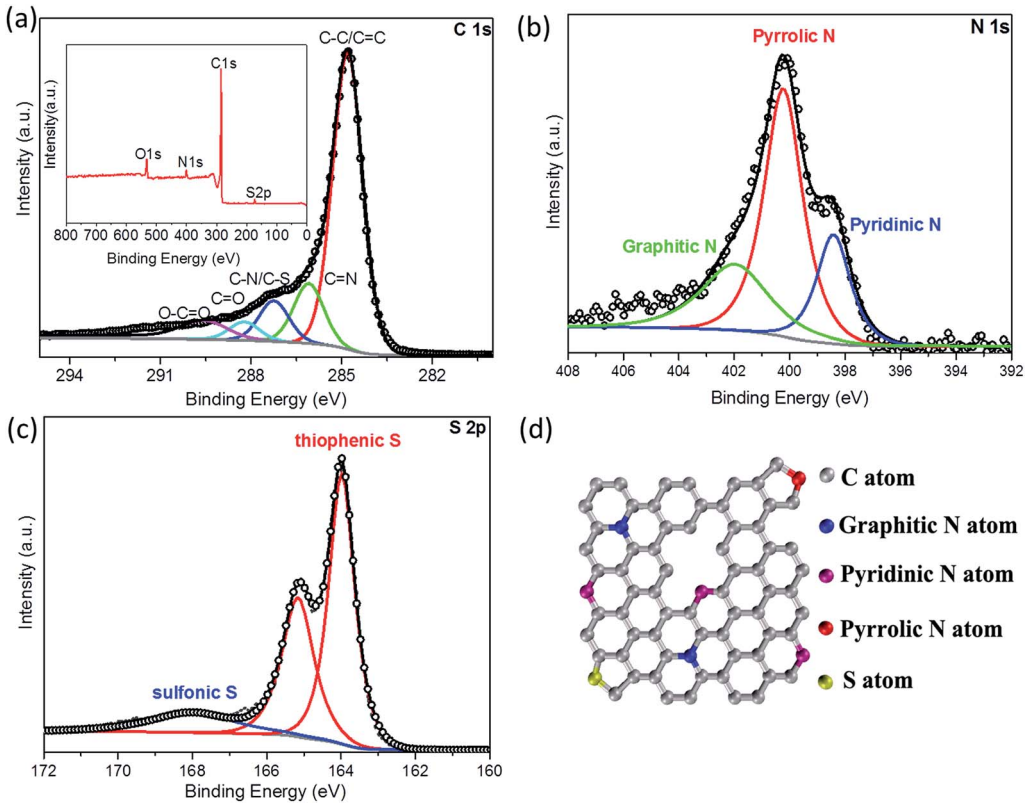

Fig. 4 (a–c) High-resolution C 1s, N 1s and S 2p XPS spectrum of A-NSG and corresponding XPS survey spectra of A-NSG. (d) Schematic structure of A-NSG.

terminal Li atom in lithium (poly)sulfides. Similarly, as indicated by Fig. S5b and d,† pyrrolic N played an analogous role as pyridinic N, which were consistent with Hou *et al.*'s theoretical results.[44] In addition, the dependence of adsorption strength between LiPSs and N doping configuration can be seen from Li–N distances. The Li–N distances of Li_2S on pyridinic and pyrrolic N sites were 1.99 and 2.02 Å, which are consistent with the large E_a obtained from Li_2S on the pyridinic N site. In the case of Li_2S_4 on pyridinic and pyrrolic N sites, the Li–N distances were calculated to be about 2.04 and 2.05 Å, which further confirmed the strong anchoring effect between pyridinic, pyrrolic N and acid terminated Li in Li_2S_x. On the other hand, in the high resolution C 1s spectra (Fig. 4a), due to the removal of most oxygen groups as well as the partial reconstruction of the graphitic carbon network, peaks corresponding to C–O (286.2 eV), C=O (288.2 eV) and O–C=O (289.6 eV)[21] decrease considerably for A-NSG, compared with that of GO;[7] two particular new peaks located at 286.1 and 287.2 eV suggest the bond formation of graphene; the sharp peak in the C 1s spectrum of A-NSG, still attributed to the sp^2-hybridized graphitic carbon atoms, shifts to higher binding energy and its full width of half-maximum (fwhm) at 284.8 eV increases with the presence of nitrogen content (Table S1, ESI†).[31,32,41] All of these results confirm the formation of C–N bonding configurations in the A-NSG. Moreover, in the X-ray photoelectron spectroscopy (XPS) analysis, the S 2p spectrum for the A-NSG nanocomposites in Fig. 4c has $2p_{3/2}$ and $2p_{1/2}$ spin–orbit levels with an energy separation of 1.27 eV and intensity ratio of 2 : 1, confirming the effective doping of sulfur atom into the carbon lattice. Two sulfur species are assigned to carbon-bonding: thiophenic S (163.6 eV) and sulfonic S (167.9 eV); the thiophenic S (sulfur atom bonded with carbon directly by a C–S bond) is believed to make the carbon matrix positively charged, thereby increasing its affinity to absorb polysulfides. At the same time, it is also interesting to find that the C/O ratio of GO is 2.4 and this value increases to 17.52 for A-NSG (Table S2, ESI†), indicating that nitrogen–sulfur co-doping increases the reduction efficiency of GO. This seems to be further supported by the Raman spectroscopy analysis. In Fig. 5a the Raman spectra for A-NSG exhibit two remarkable peaks at around 1350 and 1580 cm^{-1}. The G band located at 1580 cm^{-1} is related to the E_{2g} vibration mode of sp^2 carbon atoms while the D band at 1350 cm^{-1} is attributed to the defects and disorder hybridized vibrational mode of graphene. Therefore, the higher intensity ratio (I_D/I_G) of A-NSG than GO (1.41 *vs.* 1.06) should be ascribed to more defect sites generated by N and S co-doping, resulting in the high disorder of graphene nanosheets. More importantly, these defects can provide considerable active sites for lithium polysulfide adsorption.[21,33,40]

To further prove the interaction between polysulfides and A-NSG, the Li_2S_4 solution was prepared by dissolving Li_2S and sublimed sulfur (with a stoichiometric ratio of 1 : 3) in the mixed solvents of 1,3-dioxolane (DOL) and 1,2-dimethoxyethane (DME) (1 : 1 v/v). Then, 15 mg of N–S co-doped graphene was soaked in 15 mL of 5 mM Li_2S_4 solutions at 30 °C for 24 h,

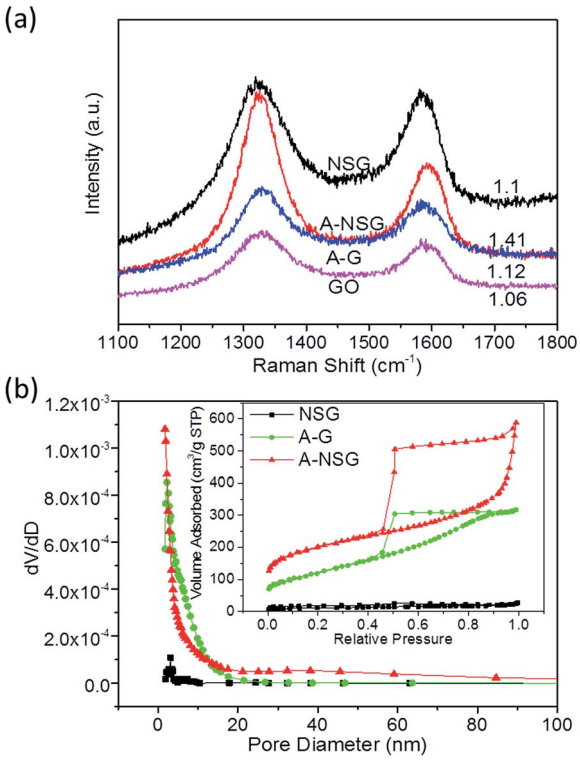

Fig. 5 (a) Raman spectra of GO, NSG, A-G and A-NSG. (b) Pore characterization of the NSG, A-G and A-NSG materials.

respectively. The upper solution was carefully collected and sealed for UV-vis spectra measurement. Fig. S6a–d (ESI†) display digital photos of pristine Li_2S_4 solution and the color changes of the Li_2S_4 solution at various periods after adding N–S co-doped graphene composites. After adding N–S co-doped graphene into the Li_2S_4 solution, a homogeneous black suspension was initially formed, and it took several minutes for N–S co-doped graphene to precipitate. After aging for 3 and 24 h, the color of Li_2S_4 turns from the initial yellow to light yellow, indicating that much of the Li_2S_4 has been adsorbed by the N, S graphene. The result indicates the adsorption capability of N–S co-doped graphene for lithium polysulfides. The corresponding UV-vis spectra in Fig. S7 (ESI†) shows that the reflect index at 533 nm of the Li_2S_4 solution was increased after soaking the N, S graphene composite for 24 h, confirming that large amount of Li_2S_4 was absorbed by N–S co-doped graphene.

We also conducted X-ray photoelectron spectroscopy (XPS) analysis to identify the interaction between polysulfides and N, S-graphene. Fig. S8a (ESI†) shows the Li 1s XPS spectrum of the electrode after discharging to 2.1 V. It exhibits a single asymmetric peak at around 56.0 eV. Therefore, an additional peak with a +1.1 eV shift was fitted and attributed to the Li in the polysulfides interacting with doped N (Li–N) because normally, the Li 1s XPS spectrum only shows the symmetric peak around 55.5 eV. This result is consistent with the observation for nitrogen/sulfur-doped cellulose bonded LiPSs,[57] suggesting that N, S doped graphene can trap the polysulphides. The S 2p spectrum also confirms the interaction between the lithium polysulfide and N–S co-doped graphene. The new peak at around 164.6 eV could be ascribed to the –C=S– bonding, which is derived from the interaction between polysulfide and the N, S doped graphene because this peak was not detected in the S 2p spectrum of N–S co-doped graphene@S (Fig. S9, ESI†).[58] This further proved the interaction between polysulfide and the N–S co-doped graphene. We also note that the peaks at 170.64 eV and 169.4 eV in the N, S co-doped graphene electrode discharged to 2.1 V (Fig. S8b, ESI†) could originate from (i) surface oxy-group of graphene and (ii) oxidization due to the exposure to the atmosphere during the transferring to the XPS measurement.

To further confirm and quantitatively characterize the polysulfide adsorption ability of N–S co-doped graphene, N doped graphene and none doped graphene, we carried out quantum mechanical calculations based on density functional theory, the results are shown in Table S3,† and the corresponding models for N–S co-doped graphene and none doped graphene are in Fig. 6, and for N-doped graphene in Fig. S5 (ESI†). The adsorption energies of Li_2S and Li_2S_4 on pristine graphene are −0.94 and −0.49 eV, respectively. The adsorption energies of Li_2S and Li_2S_4 on N doped graphene are around −1.41 and −1.01 eV, respectively, while for Li_2S and Li_2S_4 on N, S co-doped graphene, our DFT calculations predict that thiophene-like sulfur can exist adjacent to pyridinic N, as shown in Fig. 6c and d. The adsorption energies are −1.85 and −1.25 eV, respectively, which exhibits much stronger bonding effects than those on pristine graphene and N doped graphene. Furthermore, there are 0.227 and 0.019 electrons transferred from Li_2S and Li_2S_4 to pristine graphene while 0.555 and 0.317 electrons are transferred from Li_2S and Li_2S_4 to N, S co-doped graphene, suggesting that more charge migrates into co-doped graphene as lithiation proceeds.[43,44] Therefore, the co-doping of N and S in graphene can significantly enhance the adsorption of lithium polysulphides as well as lithium sulfides.

The Brunauer–Emmett–Teller (BET) results also elucidate the function of K_2CO_3 chemical activation. As shown in Fig. 5b, the optimized A-NSG showed a high BET surface area of 1012 $m^2\ g^{-1}$ and a large pore volume of 1.8 $cm^3\ g^{-1}$. A hierarchical nanoporosity including both micropores (2 nm) and mesopores (25–40 nm) resulted from the gas evolution upon pyrolysis of the polymers and K_2CO_3 chemical activation. In contrast, the NSG sample, which only experienced a nitrogen–sulfur co-doping process without K_2CO_3 chemical activation, exhibits a low surface area of 230 $m^2\ g^{-1}$ and a pore volume of 0.3 $cm^3\ g^{-1}$. Therefore, the K_2CO_3 chemical activation greatly contributes to the nanoporosity of the material. Moreover, the large pore volume plays a vital role in embedding sulfur efficiently and providing enough void space for volume expansion, while the high surface area is important for interfacial chemisorption of lithium polysulfides. On the other hand, the I_D/I_G intensity ratio of A-G of Raman spectrum analysis is clearly higher than that of GO or NSG (1.12 *vs.* 1.06, 1.1), which indicates that K_2CO_3 activation could also induce GO to generate more defects for effective reactions. In summary, the activation by K_2CO_3 yields a high BET surface area, and creates porous structures and continuous 3D networks.

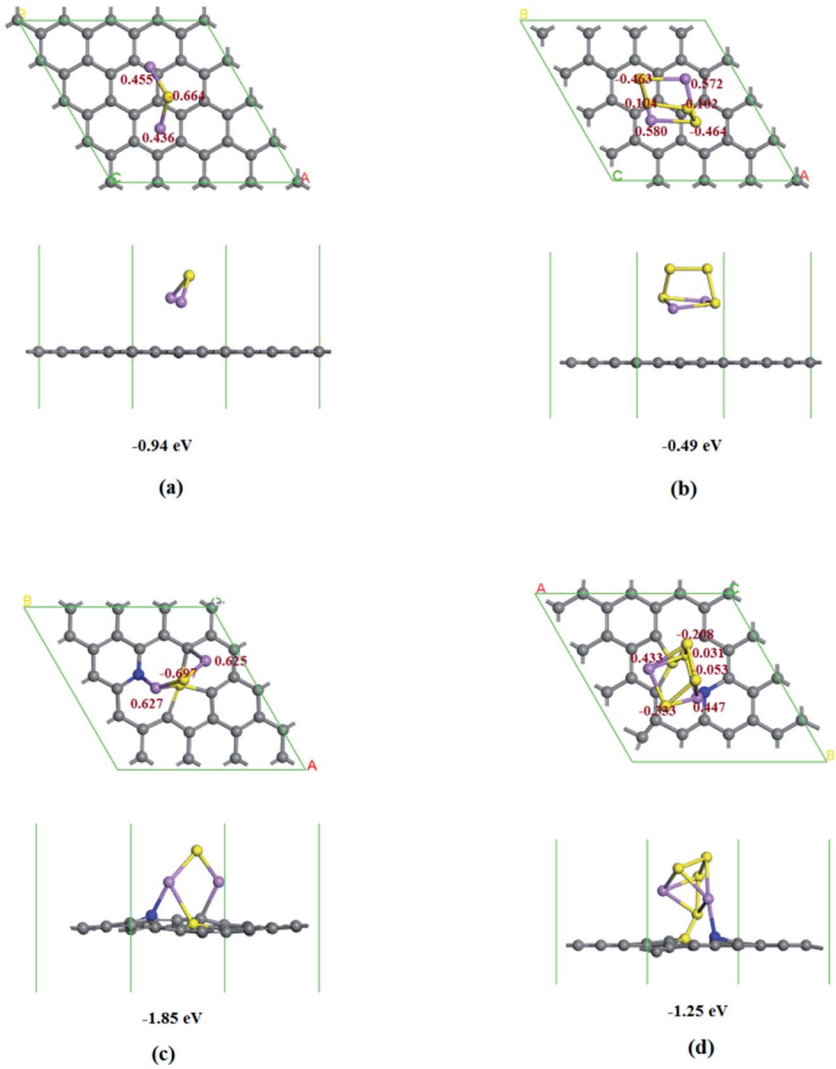

Fig. 6 Optimized configurations for the adsorption of Li_2S and Li_2S_4 on pristine graphene (a and b) and N, S codoped graphene (c and d) with corresponding adsorption energies in eV and atom Mulliken charge. Gray, blue, yellow, and purple balls represent C, N, S, and Li atoms, respectively.

The electrochemical performance of A-NSG@S nanocomposite electrodes was tested by cyclic voltammetry (CV) and charge/discharge cycling behaviors of sulfur cathodes. Two cathodic peaks at 2.35 V and 2.05 V (Fig. 7a) are consistent with the voltage plateaus in Fig. 7b. The upper plateau at 2.35 V contributes to the transformation of cyclo-octasulfur to long-chain soluble lithium polysulfides. The lower plateau at 2.05 V is associated with the decomposition of those polysulfides to insoluble short-chain lithium sulfides, which contributes to the major capacity of the A-NSG@S electrode. Notably, there are no shape or position changes of the redox peaks, implying excellent reversibility and stability of the A-NSG@S nanocomposite electrodes.[34,35] Fig. 7d shows the long-term cycling performance of the A-NSG@S at 0.2C up to 600 cycles. The electrode delivered an initial capacity of 1178 mA h g^{-1} and retained a high capacity of 780 mA h g^{-1} after 600 cycles. It should be noted that the capacity gradually increases in the first 10 cycles upon cycling at 0.2C current rate, which has been reported as a common phenomenon for electrodes applied in lithium–sulfur batteries.[45,46] As shown in Fig. 7c and d, the total capacity increased is mainly derived from the capacity accumulated in the low voltage plateau. There is almost no polysulfide loss in the high voltage plateau during the first few cycles. Normally, for sulfur batteries, the capacity is gradually decreased due to the dissolution of polysulfides at the low voltage plateau. However, due to the strong polysulfide absorption effect of N–S co-doping A-NSG, the polysulfides could be effectively trapped by the N–S co-doping graphene. Additionally, we suppose that not all sulfur takes part in the reaction with lithium ions due to the poor conductivity in the initial several cycles, and because of the "sulfur activation" in the first initial cycles,[47] more and more sulfur participated in the discharge reaction step by step, thus the capacity generated in the low voltage plateau gradually improved, resulting in the increase of total capacity. Furthermore, the capacity experienced only a slight decrease during the 100th to 600th cycles, which further demonstrates long term

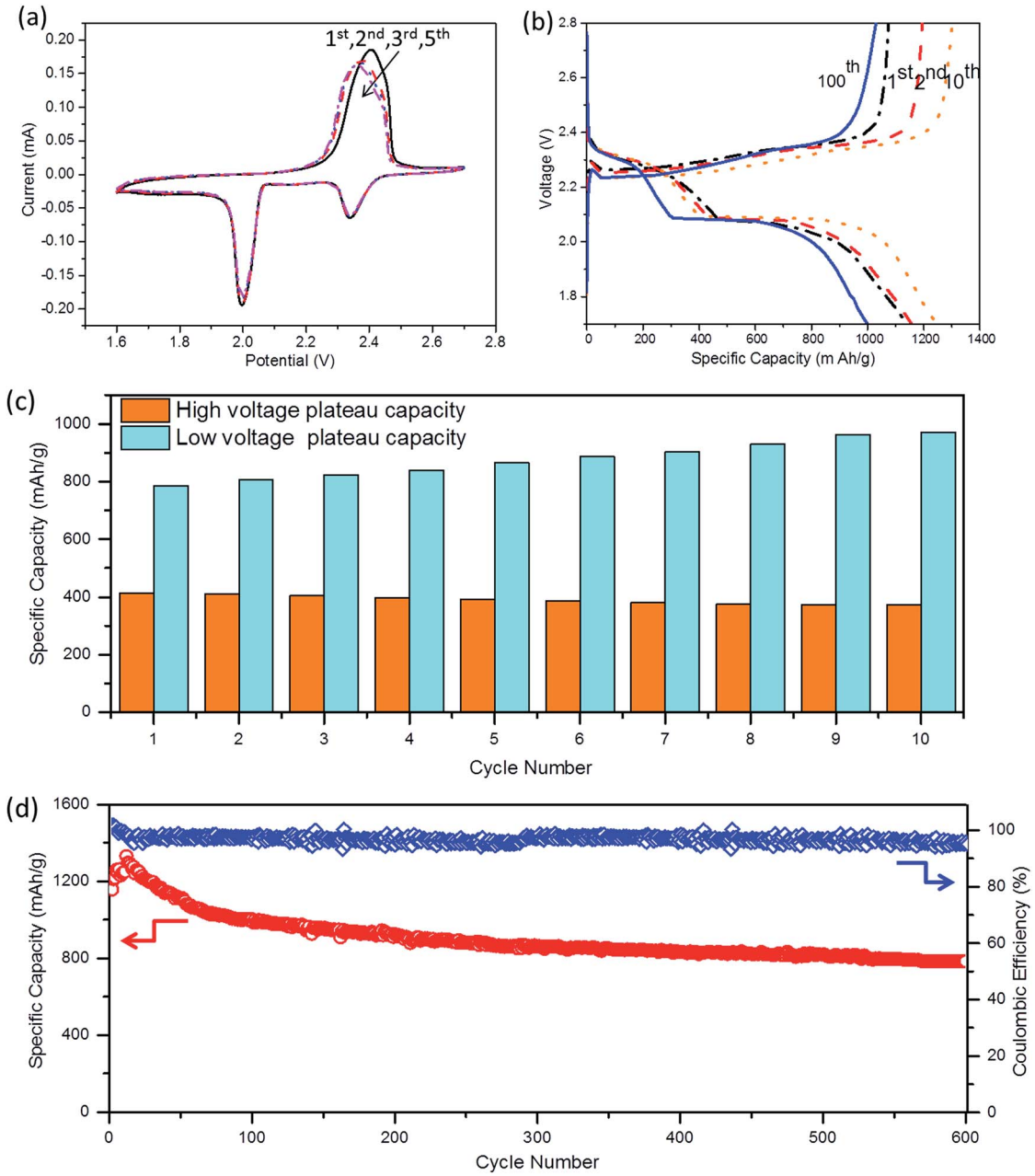

Fig. 7 Electrochemical characterization of the A-NSG material as the cathode of the Li–S battery. (a) Cyclic voltammetry (CV) measured between 1.7 and 2.7 V at a sweep rate of 0.1 mV s^{-1} for the first, second, third, and fifth cycles. (b) Galvanostatic charge and discharge profiles for different cycles at 0.2C. (c) The discharge capacities of high and low voltage plateaus. The onset voltage of the low plateau was defined around 2.0 V. (d) Long term cycling performance test of the A-NSG@S electrode at 0.2C discharge rate and the corresponding coulombic efficiency.

cycling stability. When increasing the current rates to 1C (Fig. S10, ESI†), the A-NSG@S electrodes achieved a capacity of 994 mA h g^{-1} in the initial cycle, and showed superior cycling performance with the capacity degradation rate of 0.81% per cycle up to 300 cycles. The cycling performance is much better than that of the previously reported data with high-loaded sulfur cathodes.

The high conductivity and porous structure enables the A-NSG@S composites to be kinetically sustainable for a wide range of current rates. Generally, the rate performance of a battery can be reflected from two characteristics *i.e.* the capacity maintenance at stepped rates and polarization during high-current charge and discharge processes. To explore the rate performance of A-NSG@S cathodes, we tested batteries at different current rates. The voltage gap between charge and discharge plateaus was slightly enlarged when the current rate was increased tenfold, and was stable for 200 cycles (Fig. 8b). When increasing current rates, reversible capacities of 1203, 1120, 987, and 855 mA h g^{-1} were obtained at current rates of 0.1C, 0.5C, 1C, and 2C (Fig. 8c), respectively. Even at a high

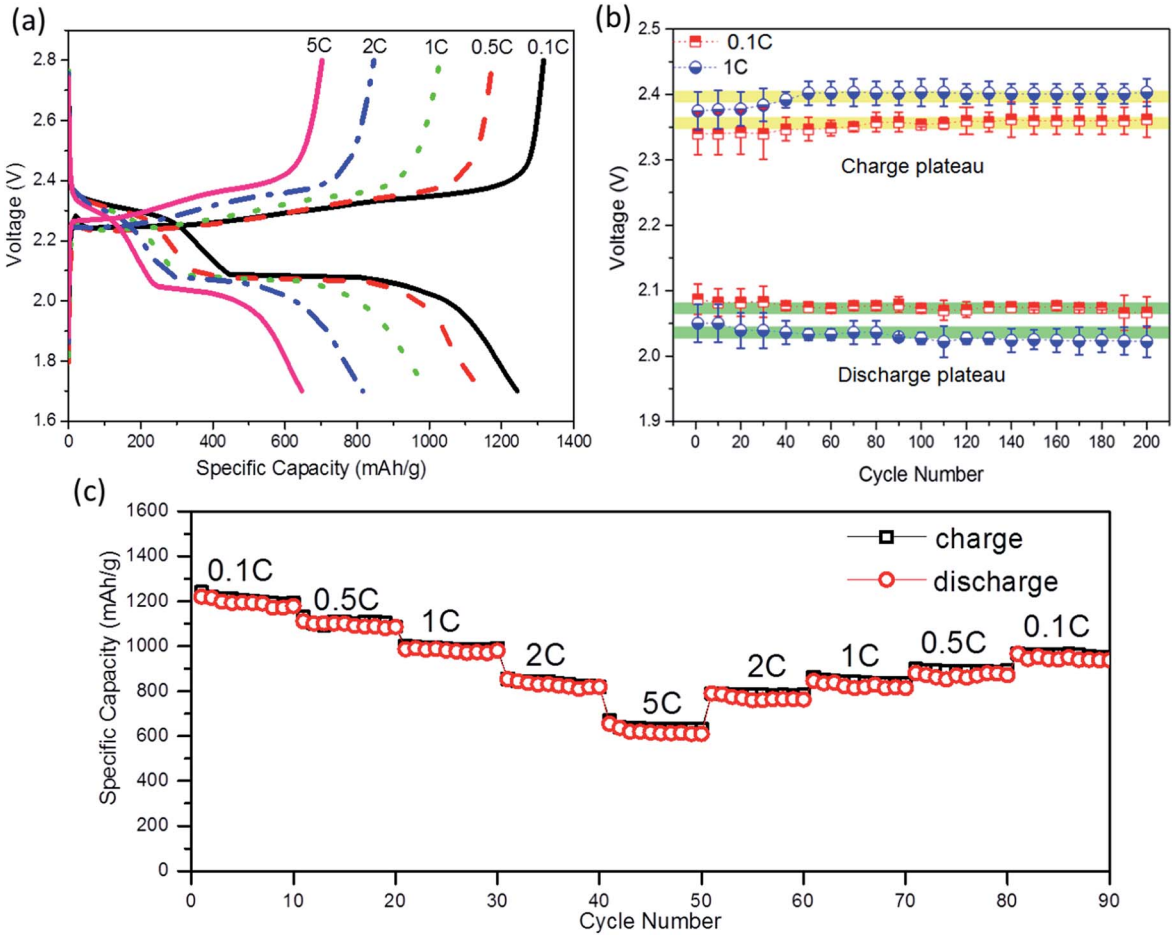

Fig. 8 Electrochemical characterization of the A-NSG material as the cathode of the Li–S battery. (a) Galvanostatic charge and discharge profiles at 0.1C, 0.5C, 1C, 2C, and 5C. (b) Voltage plateaus for charge and discharge processes over 200 cycles at 0.1 and 1C. (c) Discharge/charge capacity cycled at various rates from 0.1C, 0.5C, 1C, 2C, and 5C.

current rate of 5C, a reversible capacity of 651 mA h g^{-1} was still retained. When the current rate was gradually returned back to 0.1C, a reversible capacity of 1021 mA h g^{-1} was recovered, showing excellent high rate capability.

The Incremental Capacity Analysis (ICA) allows us to probe any gradual changes in the electrochemical behavior of rechargeable batteries during a cycle-life test with greater sensitivity than those based on the conventional charge and discharge curves. The advantage of ICA is achieved by transforming either the voltage or inflection points on *V vs. Q* curves into clearly identifiable $\Delta Q/\Delta V$ peaks on the ICA curves, depicting the solid solution or phase transformation characteristics.[36,37] By monitoring the evolution of these $\Delta Q/\Delta V$ peaks upon cycling, we can access key information on the cell chemistry behavior. Fig. 9a shows the incremental capacity peaks derived from the discharge curves (0.2C) for different cycles. The ICA peak located at 2.05 V is slightly broadened upon cycling, suggesting that the characteristics of charge transfer might have been altered, which may be associated with an increased diffusion path for lithium polysulfides due to the volume expansion during cycling. However, this voltage vibration caused by volume expansion is almost negligible compared with other reports,[23,27] because our 3D porous graphene networks and graphene layers can buffer the volume expansion/contraction of activated materials upon cycling. Meanwhile, both positions of the two peaks remain almost unchanged, implying that polarization is almost unchanged for 600 cycles. This result is consistent with the outcomes shown in Fig. 8b and 9b. Moreover, although a slight intensity reduction appears in both peaks due to the inevitable active material loss, the position as well as the sharpness of both peaks is maintained unchanged for 600 cycles, which further confirms that electrode materials preserve excellent electrochemical stability. In particular, the chemically activated A-NSG@S functions as a 3D immobilizer to accommodate a large amount of S active materials, and the internal graphene layer greatly increases the polysulfide utilization due to the improved overall electrical conductivity of the structure.

To further understand the improved electrochemical performance of A-NSG@S composites, electrochemical impedance spectroscopy (EIS) was employed to characterize the cathode before cycling, after the first cycle and 600 cycles. Nyquist plots are shown in Fig. 9b. For the cathode before cycling, the impedance curve is composed of one depressed

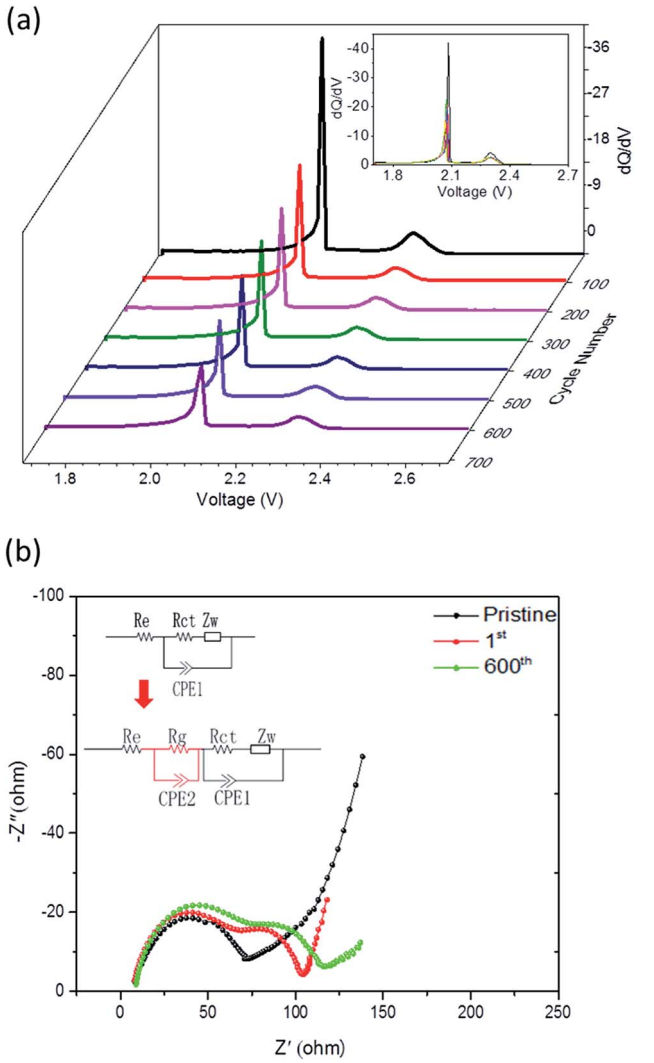

Fig. 9 (a) dQ/dV plots of the A-NSG@S electrode. (b) Electrochemical impedance spectra of the A-NSG@S lithium–sulfur battery at different cycles.

semicircle at high frequency and a short inclined line in the low frequency regions. The semicircle corresponds to the internal resistance of the cathode including bulk impedance and interfacial impedance. In addition, the inclined line at low frequency reflects the lithium ion diffusion into the active mass.[38,39] In contrast, the cathode after cycling exhibited two depressed semicircles followed by a long sloping line. The depressed semicircle in the high frequency region represents the charge transfer process at the carbon matrix interface, which also dominates the reduction reaction along the upper voltage plateau, while the semicircle at middle frequencies could be ascribed to the formation of insoluble Li_2S, Li_2S_2, which controls the lower voltage plateau.[13,40] Based on this analysis, the two features of impedance spectra in Fig. 9b can be used to deduce the equivalent circuits 1 and 2, respectively (shown as the inset). In the equivalent circuits, R_e represents the resistance of the electrolyte, R_{ct} is the charge transfer resistance at the conductive agent interface, and CPE is a constant phase element, which is associated with the roughness of the particle surface. CPE2 describes the space charge capacitance of the Li_2S (or Li_2S_2) film and R_g is the resistance in the Li_2S (or Li_2S_2) film. Z_W is the Warburg impedance due to the diffusion of the polysulfides within the cathode. The fitting results are shown in Fig. 9b. Parameter identification results are summarized in Table S4 (ESI†), according to the equivalent circuit. It can be seen that R_e experienced a slight increase during cycling due to the inevitable dissolution of polysulfides. In contrast, R_g increased remarkably during the first cycle, compared with that of a pristine cell, while it shows a modest rise in the following cycles. We can draw a conclusion that the solid Li_2S (or Li_2S_2) appeared at the very beginning of the second voltage plateau, but due to the dominant pyridinic and pyrrolic N in the carbon lattice of A-NSG@S, the electron distribution is modified and the affinity for insoluble Li_2S is improved, and the reversible conversion of Li_2S/polysulfide/S is correspondingly promoted. Similarly, R_{ct} exhibits the same trend as R_g during cycling. As for the equivalent component CPE2, which contains two parameters Y and n, the dimension for Y is $\Omega^{-1}\ cm^{-2}\ s^{-n}$ or $S\ cm^{-2}\ s^{-n}$, and the parameter n is a dimensionless index. The admittance response expression for CPE is:

$$Y = Y_0\omega n \cos(n\pi/2) + j\,Y_0\omega n \sin(n\pi/2) \quad (1)$$

However, after 600 cycles, both Y and n mostly remained stable as shown in Table S4 (ESI†), showing that the electrochemical stability of CPE2 is excellent after 600 cycles. Most importantly, this electrochemical stability also contributes greatly for the improvement of the electrochemical performance of lithium–sulfur batteries.

To demonstrate whether the co-doped heteroatoms of N and S and the graphene chemically activated by K_2CO_3 have positive functions on the electrochemical performance of Li–S batteries, several other comparison materials were prepared and tested. These include sulfur composites with about 70 wt% of sulfur prepared *via* a two step melt-diffusion method to produce nitrogen–sulfur co-doped graphene (NSG), K_2CO_3 activated graphene (A-G), nitrogen–sulfur co-doped and K_2CO_3 activated graphene (A-NSG), and graphene (rGO), denoted as NSG@S, A-G@S, A-NSG@S, and rGO@S, respectively. For comparison, the cycle performances of these electrodes were tested at the same current density, 0.2C rate, within a voltage window of 1.7–2.7 V, as shown in Fig. S11 and S12 (ESI†). The capacity retention for rGO@S, NSG@S and A-G@S electrodes up to 100 cycles is 38%, 55.2%, and 56.8%, respectively, which is not comparable with that of A-NSG@S. It also further confirmed the effective function of co-doping as well as K_2CO_3 activation. Furthermore, we compared the stability of A-NSG@S with other co-doped hosts as shown in Table S5.†[48–52] Apparently, the sulfur electrode made of A-NSG exhibits a decay rate of 0.056% per cycle up to 600 cycles, which it superior to that of other co-doped hosts. Additionally, we can see that the cycle performance of the N, S doped carbon framework is better than that of N, O doped. This is because that N and S co-doped carbon exhibits asymmetric charge density distribution, namely, N bears a negative charge and S bears a positive charge, which

benefits charge transfer.[52,56] Therefore, the excellent electrochemical performance of the A-NSG@S electrodes is clearly associated with their unique structure: (i) the 3D porous graphene network and graphene layers facilitate electron transfer, and remarkably buffer the volume expansion/contraction of active materials upon cycling. (ii) The inner defects, edges and porous structure not only permit a high sulfur loading in a homogeneously dispersed amorphous state, but also are beneficial for electrolyte access to the active sulfur component, leading to efficient reactions with Li^+. (iii) Combined physical adsorption of lithium polysulfides onto porous graphene and the chemical binding of polysulfides to N and S sites in the A-NSG promote reversible Li_2S/polysulfide/S conversion, realizing high performance Li–S batteries with long cycle life and high-energy density.

Conclusions

In summary, we designed an efficient strategy for preparing crumpled N–S co-doped porous graphene (A-NSG) *via* chemical activation of polypyrrole (PPy) functionalized graphene sheets with K_2CO_3. The A-NSG@S electrodes with a high sulfur loading of 72.4 wt% exhibit low polarization, stable cycling performance, and excellent rate capability, compared with rGO@S, NSG@S and A-G@S electrodes. The excellent performance could be attributed to synergic effects, including the high surface area and high conductivity of the porous matrix, as well as the unique lithium polysulfide binding capability of the N, S functional groups in the A-NSG sheets. Furthermore, pyridinic nitrogen and thiophenic sulfur in the carbon lattice of A-NSG@S can modify the electron distribution and improve the affinity for Li_2S as well as Li_2S_4, leading to the improvement in reversibility of Li_2S/polysulfide/S conversion. This work not only presents a simple method to synthesize N–S co-doped hierarchical porous graphene, but also demonstrates the excellent performance of A-NSG cathode materials for lithium–sulfur batteries.

Acknowledgements

This project is financially supported by the Australian Renewable Energy Agency (ARENA) through an ARENA project (ARENA 2014/RND106). The author Jing Xu gratefully acknowledges the support from the Chinese Scholarship Council (CSC, No. 201307090011).

Notes and references

1 A. Manthiram, S. H. Chung and C. Zu, *Adv. Mater.*, 2015, **27**, 1980–2006.
2 X. Fang, W. Weng, J. Ren and H. Peng, *Adv. Mater.*, 2016, **28**, 491–496.
3 L. Qie, C. Zu and A. Manthiram, *Adv. Energy Mater.*, 2016, **7**, 23–25.
4 H. Kim, J. Lee, H. Ahn, O. Kim and M. J. Park, *Nat. Commun.*, 2015, **6**, 7278.
5 H. Chen, Q. Zou, Z. Liang, H. Liu, Q. Li and Y. C. Lu, *Nat. Commun.*, 2015, **6**, 5877.
6 W. Li, H. Yao, K. Yan, G. Zheng, Z. Liang, Y. M. Chiang and Y. Cui, *Nat. Commun.*, 2015, **6**, 7436.
7 G. Zhou, E. Paek, G. S. Hwang and A. Manthiram, *Nat. Commun.*, 2015, **6**, 7760.
8 H. Chen, C. Wang, C. Hu, J. Zhang, S. Gao, W. Lu and L. Chen, *J. Mater. Chem. A*, 2015, **3**, 1392–1395.
9 Z. Ma, S. Dou, A. Shen, L. Tao, L. Dai and S. Wang, *Angew. Chem.*, 2015, **54**, 1888–1892.
10 M. Wang, H. Zhang, Q. Wang, C. Qu, X. Li and H. Zhang, *ACS Appl. Mater. Interfaces*, 2015, **7**, 3590–3599.
11 Q. Sun, X. Fang, W. Weng, J. Deng, P. Chen, J. Ren, G. Guan, M. Wang and H. Peng, *Angew. Chem.*, 2015, **54**, 10539–10544.
12 X. Zhao, H. J. Ahn, K. W. Kim, K. K. Cho and J. H. Ahn, *J. Phys. Chem. C*, 2015, **119**, 7996–8003.
13 X. Liang, A. Garsuch and L. F. Nazar, *Angew. Chem.*, 2015, **54**, 3907–3911.
14 J. Song, M. L. Gordin, T. Xu, S. Chen, Z. Yu, H. Sohn, J. Lu, Y. Ren, Y. Duan and D. Wang, *Angew. Chem.*, 2015, **54**, 4325–4329.
15 S. Xiao, S. Liu, J. Zhang and Y. Wang, *J. Power Sources*, 2015, **293**, 119–126.
16 P. Strubel, S. Thieme, T. Biemelt, A. Helmer, M. Oschatz, J. Brückner, H. Althues and S. Kaskel, *Adv. Funct. Mater.*, 2015, **25**, 287–297.
17 X. G. Sun, Y. Fang, X. Jiang, K. Yoshii, T. Tsuda and S. Dai, *Chem. Commun.*, 2016, **52**, 292–295.
18 M. Rao, X. Geng, X. Li, S. Hu and W. Li, *J. Power Sources*, 2012, **212**, 179–185.
19 M. Liu, D. Zhou, Y. B. He, Y. Fu, X. Qin, C. Miao, H. Du, B. Li, Q. H. Yang, Z. Lin, T. S. Zhao and F. Kang, *Nano Energy*, 2016, **22**, 278–289.
20 Y. Y. L. Ding, P. Kopold, K. Hahn, P. A. van Aken, J. Maier and Y. Yu, *Adv. Funct. Mater.*, 2015, **34**, 578–584.
21 Q. Pang, J. Tang, H. Huang, X. Liang, C. Hart, K. C. Tam and L. F. Nazar, *Adv. Mater.*, 2015, **27**, 6021–6028.
22 Y. Qiu, W. Li, W. Zhao, G. Li, Y. Hou, M. Liu, L. Zhou, F. Ye, H. Li, Z. Wei, S. Yang, W. Duan, Y. Ye, J. Guo and Y. Zhang, *Nano Lett.*, 2014, **14**, 4821–4827.
23 L. Fei, X. Li, W. Bi, Z. Zhuo, W. Wei, L. Sun, W. Lu, X. Wu, K. Xie, C. Wu, H. L. Chan and Y. Wang, *Adv. Mater.*, 2015, **27**, 5936–5942.
24 L. Ji, M. Rao, H. Zheng, L. Zhang, Y. Li, W. Duan, J. Guo, E. J. Cairns and Y. Zhang, *J. Am. Chem. Soc.*, 2011, **133**, 18522–18525.
25 J. P. Rong, M. Y. Ge, X. Fang and C. W. Zhou, *Nano Lett.*, 2014, **14**, 473–479.
26 M. Agostini, B. Scrosati and J. Hassoun, *Adv. Energy Mater.*, 2015, **78**, 785–793.
27 Y. W. Zhu, S. Murali, M. D. Stoller, K. J. Ganesh, W. W. Cai and P. J. Ferreira, *Science*, 2011, **332**(6037), 1537–1541.
28 Y. Xi, Z. Long, Z. Fan and H. Yi, *ACS Nano*, 2014, **8**(5), 5208–5215.
29 C. Zu and A. Manthiram, *Adv. Energy Mater.*, 2014, **4**(18), 6784–6789.
30 Z. Li and L. Yin, *ACS Appl. Mater. Interfaces*, 2015, **7**, 4029–4038.

31 S. Zhen, S. Lin, C. Jing, B. Wen and W. Feng, *ACS Nano*, 2011, **5**(6), 4350–4358.
32 Y. Shao, S. Zhang, M. H. Engelhard, G. Li, G. Shao, Y. Wang, J. Liu, I. A. Aksay and Y. Lin, *J. Mater. Chem.*, 2010, **20**, 7491.
33 T. Yang, T. Qian, M. Wang, X. Shen, N. Xu, Z. Sun and C. Yan, *Adv. Mater.*, 2016, **28**, 539–545.
34 S. Chen, X. Huang, H. Liu, B. Sun, W. Yeoh, K. Li, J. Zhang and G. Wang, *Adv. Energy Mater.*, 2014, **4**, 159–165.
35 C. Wang, K. Su, W. Wan, H. Guo, H. H. Zhou, J. T. Chen, X. X. Zhang and Y. H. Huang, *J. Mater. Chem. A*, 2014, **2**, 5018–5023.
36 J. Ryu, D. Hong, S. Choi and S. Park, *ACS Nano*, 2016, **10**, 2843–2851.
37 J. Nelson, S. Misra, Y. Yang, A. Jackson, Y. J. Liu, H. L. Wang, H. J. Dai, J. C. Andrews, Y. Cui and M. F. Toney, *J. Am. Chem. Soc.*, 2012, **134**, 6337–6343.
38 C. Barchasz, J. C. Leprêtre, F. Alloin and S. Patoux, *J. Power Sources*, 2012, **199**, 322–330.
39 Z. Li, J. T. Zhang, Y. M. Chen, J. Li and X. W. Lou, *Nat. Commun.*, 2015, **6**, 8850.
40 L. Yuan, X. Qiu, L. Chen and W. Zhu, *J. Power Sources*, 2009, **189**, 127–132.
41 J. Zhang, Z. Dong, X. Wang, X. Zhao, J. Tu, Q. Su and G. Du, *J. Power Sources*, 2014, **270**, 1–8.
42 C. Xu, Y. Wu, X. Zhao, X. Wang, G. Du, J. Zhang and J. Tu, *J. Power Sources*, 2015, **275**, 22–25.
43 T. Z. Hou, X. Chen, H. J. Peng, J. Q. Huang, B. Q. Li, Q. Zhang and B. Li, *Small*, 2016, **12**, 3283–3291.
44 T.-Z. Hou, H.-J. Peng, J.-Q. Huang, Q. Zhang and B. Li, *2D Mater.*, 2015, **2**, 014011.
45 L. Miao, W. Wang, K. Yuan, Y. Yang and A. Wang, *Chem. Commun.*, 2014, **50**, 13231–13234.
46 G. Zhou, L. Li, C. Ma, S. Wang, Y. Shi, N. Koratkar, W. Ren, F. Li and H.-M. Cheng, *Nano Energy*, 2015, **11**, 356–365.
47 L.-C. Yin, J. Liang, G.-M. Zhou, F. Li, R. Saito and H.-M. Cheng, *Nano Energy*, 2016, **25**, 203–210.
48 Z. Wang, Y. Dong, H. Li, Z. Zhao, H. B. Wu, C. Hao, S. Liu, J. Qiu and X. W. Lou, *Nat. Commun.*, 2014, **5**, 5002.
49 G. Zhou, E. Paek, G. S. Hwang and A. Manthiram, *Nat. Commun.*, 2015, **6**, 7760.
50 H.-J. Peng, T.-Z. Hou, Q. Zhang, J.-Q. Huang, X.-B. Cheng, M.-Q. Guo, Z. Yuan, L.-Y. He and F. Wei, *Adv. Mater. Interfaces*, 2014, **1**, 1400227.
51 J. Song, M. L. Gordin, T. Xu, S. Chen, Z. Yu, H. Sohn, J. Lu, Y. Ren, Y. Duan and D. Wang, *Angew. Chem.*, 2015, **54**, 4325–4329.
52 Q. Pang, J. Tang, H. Huang, X. Liang, C. Hart, K. C. Tam and L. F. Nazar, *Adv. Mater.*, 2015, **27**, 6021–6028.
53 J. Guo, J. Zhang, F. Jiang, S. Zhao, Q. Su and G. Du, *Electrochim. Acta*, 2015, **176**, 853–860.
54 Y. Liu, J. Guo, J. Zhang, Q. Su and G. Du, *Appl. Surf. Sci.*, 2015, **324**, 399–404.
55 Y. Wu, C. Xu, J. Guo, Q. Su, G. Du and J. Zhang, *Mater. Lett.*, 2014, **137**, 277–280.
56 M. Hagen, P. Schiffels, M. Hammer, S. Dorfler, J. Tubke, M. J. Hoffmann, H. Althues and S. Kaskel, *J. Electrochem. Soc.*, 2013, **160**, A1205–A1214.
57 Q. Pang, J. Tang, H. Huang, X. Liang, C. Hart, K. C. Tam and L. F. Nazar, *Adv. Mater.*, 2015, **27**, 6021–6028.
58 Y. Ito, W. Cong, T. Fujita, Z. Tang and M. Chen, *Angew. Chem.*, 2015, **54**, 2131–2136.